



# 1 Global GOSAT, OCO-2 and OCO-3 Solar Induced Chlorophyll

## 2 Fluorescence Datasets

3 Russell Doughty<sup>1\*</sup>, Thomas Kurosu<sup>2</sup>, Nicholas Parazoo<sup>2</sup>, Philipp Köhler<sup>1</sup>, Yujie Wang<sup>1</sup>, Ying  
4 Sun<sup>3</sup>, Christian Frankenberg<sup>1,2</sup>

5 <sup>1</sup> Division of Geological and Planetary Sciences, California Institute of Technology, Pasadena, CA, 91125, USA

6 <sup>2</sup> Jet Propulsion Laboratory, Tropospheric Composition, Pasadena, CA, 91109, USA

7 <sup>3</sup> Soil and Crop Sciences Section, School of Integrative Plant Science, Cornell University, Ithaca, NY, 14853, USA

8 *Correspondence to:* Russell Doughty (rdoughty@caltech.edu)

9 **Abstract.** The retrieval of solar induced chlorophyll fluorescence (SIF) from space is a relatively new  
10 advance in Earth observation science, having only become feasible within the last decade. Interest in SIF  
11 data has grown exponentially, and the retrieval of SIF and the provision of SIF data products has become  
12 an important and formal component of spaceborne Earth observation missions. Here, we describe the global  
13 Level 2 SIF Lite data products for the Greenhouse Gases Observing Satellite (GOSAT), the Orbiting  
14 Carbon Observatory-2 (OCO-2), and OCO-3 platforms, which are provided for each platform in daily  
15 netCDF files. We also outline the methods used to retrieve SIF and estimate uncertainty, describe all the  
16 data fields, and provide users the background information necessary for the proper use and interpretation  
17 of the data, such as considerations of retrieval noise, sun-sensor geometry, the indirect relationship between  
18 SIF and photosynthesis, and differences among the three platforms and their respective data products. OCO-  
19 2 and OCO-3 have the highest spatial resolution spaceborne SIF retrievals to date, and the target and  
20 snapshot area mode observation modes of OCO-2 and OCO-3 are unique. These modes provide hundreds  
21 to thousands of SIF retrievals at biologically diverse global target sites during a single overpass, and provide  
22 an opportunity to better inform our understanding of canopy-scale vegetation SIF emission across biomes.

## 23 1 Introduction

24 Chlorophyll fluorescence is light that is emitted from chlorophyll after the absorption of photosynthetically  
25 active radiation (PAR), which covers the spectral range of roughly 400 to 700 nm and corresponds to the  
26 range of light visible to the human eye. The fluorescence emission occurs in the range of ~650 to 800 nm  
27 during the light reaction of photosynthesis, where energy absorbed by leaf pigments is converted into the  
28 chemical energy that is needed by the dark reactions for fixing atmospheric carbon dioxide into sugars. The  
29 absorption of a photon by chlorophyll excites an electron, and the excitation energy has three main  
30 pathways: photochemistry, non-photochemical quenching or heat, and chlorophyll fluorescence. Most of



31 the excitation energy is used for photochemistry when vegetation is not stressed and light conditions are  
32 not extreme, but at all times only a small fraction (~0.5-2%) is emitted as chlorophyll fluorescence (Porcar-  
33 Castell et al., 2014; Maxwell and Johnson, 2000).

34

35 Chlorophyll fluorescence has been a research tool for studying photosynthesis for nearly 150 years (Müller,  
36 1874), but only recently have spaceborne retrievals of solar induced chlorophyll fluorescence (SIF) been  
37 realized (Guanter et al., 2007; Joiner et al., 2011; Frankenberg et al., 2011b). The number of spaceborne  
38 platforms from which SIF can be retrieved continues to grow, and the SIF temporal record continues to  
39 lengthen. Spaceborne SIF data has generated much excitement in a plethora of fields within the biological,  
40 biogeochemical cycle, climate, and Earth system science communities. Chlorophyll fluorescence has long  
41 been a key component of the plant physiological and ecophysiological research communities (Maxwell and  
42 Johnson, 2000) and has traditionally been studied *in vivo* at the subcellular and leaf level, and *in situ* using  
43 pulse amplitude-modulated (PAM) fluorometry (Schreiber et al., 1986).

44

45 Most recently, remote sensing techniques have enabled the canopy and ecosystem-level retrieval of SIF  
46 from towers, aircraft, and satellites. The evolution in our ability to retrieve SIF infrequently at the leaf-level  
47 to frequent canopy-level retrievals across regional to global scales continues to greatly advance our  
48 understanding of plant and ecosystem function and carbon cycling. However, there are fundamental  
49 differences between in-situ PAM fluorometry and SIF. The former measures steady-state and light-  
50 saturated fluorescence yields, which allow the derivation of photosynthetic yields (Genty et al., 1989) while  
51 the latter only measures absolute SIF, following absorption of solar light by chlorophyll. The relationship  
52 of SIF with photosynthetic yields is thus more complex (Porcar-Castell et al., 2014; Frankenberg et al.,  
53 2014; Gu et al., 2019).

54

55 Here, we describe, compare, and discuss the Level 2 SIF Lite version 10 (v10) data produced from three  
56 spaceborne platforms: the Greenhouse Gases Observing Satellite (GOSAT), the Orbiting Carbon  
57 Observatory-2 (OCO-2), and OCO-3 (OCO-2 Science Team et al., 2020; OCO-3 Science Team et al.,  
58 2020). Our data description is an update and synthesis of information that has been dispersed among several  
59 user guides, publications, and supplementary materials related to these three platforms. Our presentation  
60 and comparison of the SIF data from the three platforms and our discussions on SIF are intended to help  
61 the user community find creative ways to apply the data and prevent misinterpretation.

62

63 Level 2 data is ungridded (vector) data that contains geophysical variables that are of interest and use to the  
64 broader scientific community and is at same resolution of the Level 0 and Level 1 data, which are data

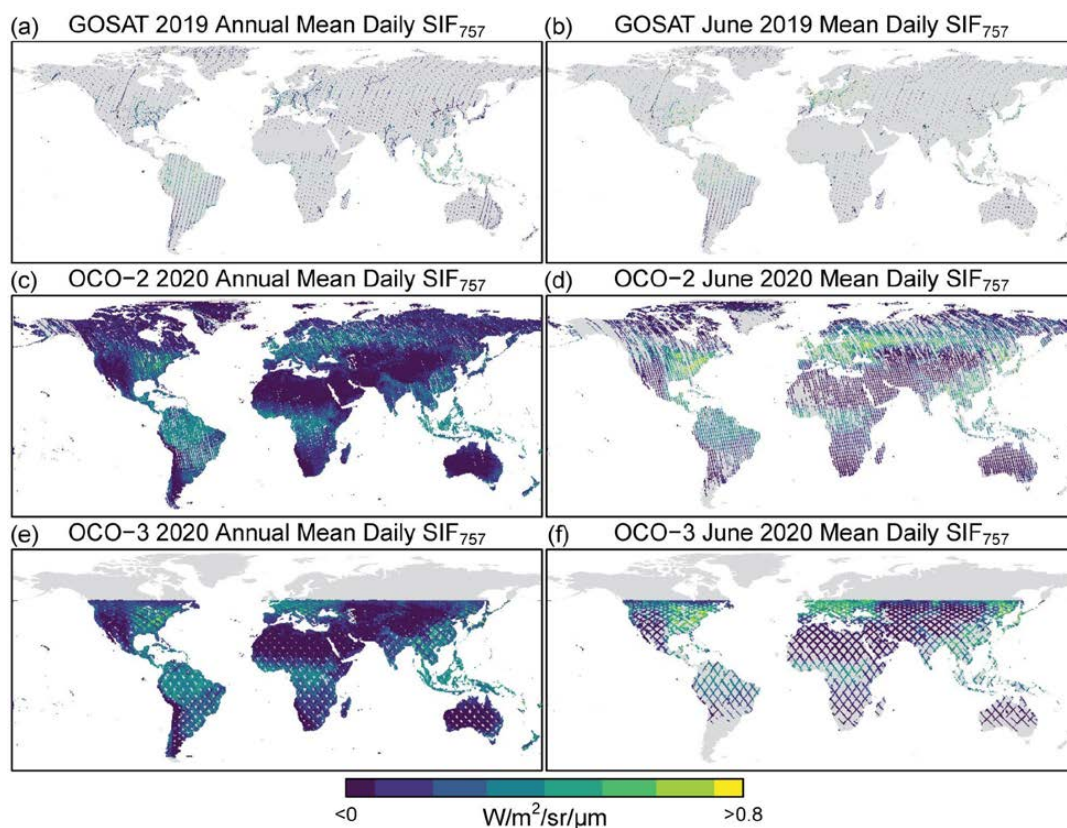


65 obtained as-is from the sensor (Level 0) to which ancillary information is appended (Level 1), such as  
66 radiometric and geometric calibration coefficients and georeferencing parameters. Level 3 products refer  
67 to gridded (raster) data, which can be found at <https://climatesciences.jpl.nasa.gov/sif/download-data/level-3/>.

68  
69

70 The annual and monthly spatial distribution of the Level 2 data for the globe and the continental United  
71 States are presented in Figures 1 and 2 for visualization. These data are produced by the OCO-2 and OCO-  
72 3 projects at the Jet Propulsion Laboratory (Frankenberg et al., 2014), quality controlled by NASA's  
73 Making Earth System Data Records for Use in Research Environments (MEaSUREs) SIF team, and are  
74 publicly available on the NASA Goddard Earth Sciences Data and Information Services Center (GES-  
75 DISC) website (<https://disc.gsfc.nasa.gov/>). Recent efforts by the OCO and MEaSUREs team have focused  
76 on harmonizing the processing pipeline, attributes, and file structures of the GOSAT and OCO SIF products  
77 (Parazoo et al., 2019). Here, we present a first analysis of these harmonized products and demonstrate for  
78 the user community their key commonalities and differences.

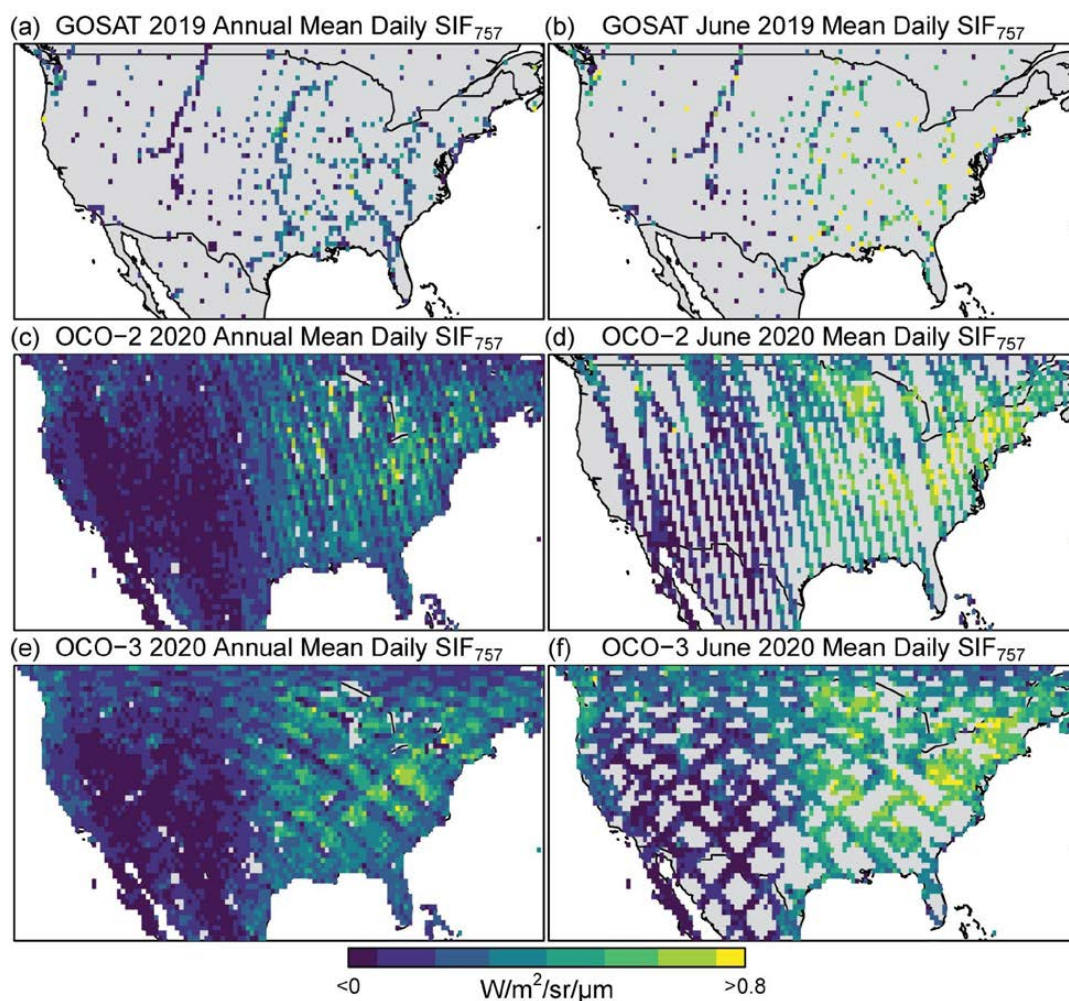
79



80



81 **Figure 1. Annual 2020 and June 2020 Mean Daily SIF<sub>757</sub> for GOSAT, OCO-2, and OCO-3.** The annual  
82 and monthly coverage of GOSAT, OCO-2, and OCO-3 is presented here as mean daily SIF at 757 nm  
83 (SIF<sub>757</sub>) at a gridded resolution of 0.5° for visualization. Included are soundings from all measurement  
84 modes flagged as *best* and *good* quality and *clear* of clouds. At nadir, the diameter of the GOSAT soundings  
85 is ~10 km, and the widths of the OCO-2 and OCO-3 swaths are about 10 km and 13 km, respectively. Thus,  
86 the data gaps shown here are larger than depicted and are not to scale.  
87



88  
89 **Figure 2. Annual 2020 and June 2020 Mean Daily SIF<sub>757</sub> for GOSAT, OCO-2, and OCO-3 for**  
90 **CONUS.** These panels are zoom-ins of the contiguous United States from Figure 1.





## 91 **2 Satellite platforms**

92 The retrieval of SIF requires high spectral resolution and a high signal to noise ratio (SNR) as solar  
93 Fraunhofer lines are very narrow and because SIF is a relatively weak signal (Frankenberg et al., 2011b).  
94 Coincidentally, the spaceborne spectrometers that have been used for retrieving Earth's atmospheric carbon  
95 dioxide and methane concentrations include spectral channels covering Fraunhofer lines in the vicinity of  
96 the oxygen A-band where atmospheric mass is retrieved with high spectral resolution ( $< 0.2$  nm), enabling  
97 SIF retrievals with single measurement precision around  $\sim 0.5$  W/m<sup>2</sup>/s/ $\mu$ m. Thus, the retrieval of SIF from  
98 space has been pioneered by the atmospheric science community (Guanter et al., 2007; Joiner et al., 2011;  
99 Frankenberg et al., 2011b), and spaceborne SIF retrievals and data products have historically been a by-  
100 product of missions that have aimed to monitor Earth's atmospheric trace gases.

### 101 **2.1 GOSAT**

102 GOSAT (aka Ibuki) was developed by the Japan Aerospace Exploration Agency (JAXA) and launched in  
103 January 2009. In fact, the first global satellite SIF observations came from GOSAT (Joiner et al., 2011;  
104 Frankenberg et al., 2011b) (Joiner et al., 2011; Frankenberg et al., 2011b). Onboard the satellite is the  
105 greenhouse gas observation sensor (TANSO-FTS), which has a spectral resolution of  $0.2$  cm<sup>-1</sup> and an  
106 oxygen A-band SNR  $> 300$ . It has a sun synchronous, descending orbit with an overpass time of  $13:00 \pm$   
107  $15$  minutes at the equator, a 3-day repeat cycle, and a circular footprint of  $\sim 82$  km<sup>2</sup> per sounding ( $\sim 10$  km  
108 diameter) (Kuze et al., 2009).

### 109 **2.2 OCO-2 and OCO-3**

110 OCO-2 is a NASA satellite that was launched in July 2014, and OCO-3 is a duplicate of the OCO-2 grating  
111 spectrometer attached to the Japanese Experimental Module Exposed Facility (JEM-EF) on the  
112 International Space Station (ISS) in May 2019 (Eldering et al., 2019). Each platform houses a 3-channel  
113 grating spectrometer with a spectral resolving power of  $\lambda/\Delta\lambda > 17,000$  and a signal-to-noise ratio of  $> 400$   
114 (Crisp et al., 2017; Eldering et al., 2019). They have three bands: an oxygen-A band at  $0.765$   $\mu$ m and carbon  
115 dioxide bands at  $1.61$   $\mu$ m and  $2.06$   $\mu$ m. The swath widths are  $\sim 10$  km with eight measurements across-  
116 track. The spatial resolution at nadir is slightly different for OCO-2 and OCO-3, about  $1.3$  km by  $2.25$  km  
117 and  $1.6$  km by  $2.2$  km, respectively.

118

119 OCO-2 has a 98.8-minute orbit with a 1:36 PM nodal crossing time and a 16-day ground-track repeat cycle  
120 (Crisp et al., 2017). The ISS has a precessing low-inclination orbit that allows OCO-3 to view Earth at  
121 absolute latitudes less than  $\sim 52^\circ$ . The ISS orbits the Earth  $\sim 15.5$  times a day and data acquisition is  
122 sometimes halted during ISS maintenance and docking, thus overpass times, revisit periods, and data



123 availability are relatively irregular. Validation of the OCO-2 SIF retrievals was conducted by Sun et al.  
124 (2017) by comparing OCO-2 SIF to coordinated airborne measurements using the Chlorophyll  
125 Fluorescence Imaging Spectrometer (Frankenberg et al., 2018).

### 126 **2.3 Observation Modes**

127 GOSAT observation modes are described as Observation Mode 1 Sunshine (OB1D), Observation Mode 2  
128 Sunshine (OB2D), and Specific Observation Mode Sunshine (SPOD). OB1D is the routine observation  
129 mode, whereas OB2D is a non-routine mode in which the thermal-infrared observation and pointing  
130 mechanism is stopped during low power supply. Over land, SPOD is a target observation mode designed  
131 to observe specific sites. The TANSO-FTS sensor has a setting for low, medium, and high gain. The  
132 medium gain data is recommended for scenes that are bright, such as deserts. Since the data used for SIF  
133 retrievals are filtered to exclude bright scenes due to deserts, ice, snow, and cloud cover, the high gain data  
134 is used for SIF retrievals.

135

136 Nadir, glint, target, and transition observation modes are common to each OCO platform. The OCO-2 target  
137 mode provides repeated spatial sampling of a given target, such as an emission source or tower site. The  
138 OCO-3 target mode is a sequence of adjacent and partially overlapping swaths that allow for increased  
139 spatial sampling. The target modes for both platforms provide over  $10^3$  soundings. OCO-3 has an additional  
140 observation mode using its pointing mirror assembly (PMA), which allows for snapshot area mapping  
141 (SAM) of targets of interest. SAMs are a series of scans of a target that are nearly adjacent and can cover  
142 an area of  $\sim 80$  km by 80 km in about 2 minutes. The SAMs and their target locations, which include  
143 volcanoes, various vegetation land cover types, and point sources of fossil fuel emissions, can be viewed at  
144 <https://ocov3.jpl.nasa.gov/sams/index.php>. Target and SAM mode scans are prioritized and scheduled days  
145 in advance of an overpass of the ISS over the target (Taylor et al., 2020).

146

147 The target and SAM observation modes offer unique, spatially resolved acquisition of a target during a  
148 single overpass at different sun-sensor geometries as solar illumination is relatively fixed during overpasses  
149 and soundings are acquired over a range of viewing angles as the sensors pass over their targets. For SIF  
150 applications, these measurements can be averaged to obtain SIF estimates with a reduced standard error or  
151 binned by sun-sensor geometries to investigate the effect of observation geometry of the retrieved SIF  
152 values, as we demonstrate below.



### 153 **3 Data description**

#### 154 **3.1 SIF Lite file structure and content**

155 The ungridded Level 2 SIF Lite data are provided in netCDF-4 format and contain information for each  
156 sounding from which a SIF retrieval was made. For each of the three satellite platforms, there is one file  
157 for each day in which there is at least one sounding and each file contains information for all soundings  
158 acquired on that day, including all measurement modes (glint, nadir, target). The SIF Lite files can be read  
159 by, but are not limited to, MATLAB, Python, R, and Julia using their respective netCDF4 or HDF5 libraries.  
160 The filename convention is, using the filename “oco2\_LtSIF\_200201\_20210129t071949z.nc4” as an  
161 example, platform (oco2), data product (LtSIF), date (YYMMDD), and file creation date (YYYYMMDD)  
162 and time (tHHMMSS). The SIF Lite netCDF global attributes, dimensions, variables, and variable groups  
163 are described below and listed in Table1.

##### 164 **3.1.1 Global attributes and dimensions**

165 The global attributes provide file-level metadata information, the most important of which for data users  
166 are the citation, contact information, and the time range of the data in the file. The times listed in the global  
167 attributes can be used in instances where the file names may have been changed. A netCDF dimension is  
168 an integer that specifies the shape of the multi-dimensional variables, and these are also described in Table  
169 1. For the OCO-2 and OCO-3 data, there are dimensions for the footprint vertices (vertex\_dim) and across-  
170 track footprint (footprint\_dim), which are not applicable for GOSAT. The polarization dimension  
171 (polarization\_dim) is used for GOSAT’s P and S polarizations. The only variable dimension is the  
172 *sounding\_dim*, which is the number of soundings in the file.

##### 173 **3.1.2 Variables**

174 The primary variables of interest in the SIF Lite files are the *SIF*, *Daily\_SIF*, and *SIF\_Uncertainty* variables,  
175 which are available for SIF retrievals at 757 nm and 771 nm and estimated SIF at 740 nm. The variables  
176 for GOSAT differ from those of OCO-2 and OCO-3 in that GOSAT has two polarizations, P and S, and  
177 thus retrieval-related variables are provided as a 2-dimensional (2D) array. It is important to note that  
178 although the SIF values have traditionally been loosely labelled as being retrieved at 757 nm and 771 nm,  
179 the retrieval fit windows used to produce the SIF Lite data is centered at 758.7 and 770.1 for OCO-2 and  
180 OCO-3, and at 758 and 771 for GOSAT. However, we retain the 757 and 771 nomenclature to remain  
181 consistent with previous publications and to avoid confusion.



### 182 3.1.3 Variable groups

183 Most of the variables have been grouped, as listed in Table 1. The ungrouped, root-level variables are those  
184 that are most used and some of these variables are duplicated in the *Geolocation* and *Science* groups. The  
185 *Cloud* group contains cloud and surface albedo variables from the L2ABP product, which are used in the  
186 assignment of the quality flag. The *Geolocation* group contains variables related to the geolocation of the  
187 sounding footprint, sun-sensor geometry, altitude, and acquisition time. GOSAT sounding footprints are  
188 circular and have a radius of 5 km, in contrast to the OCO-2 and OCO-3 soundings, which are rhomboidal  
189 and are described with coordinates for each of their four vertices. Thus, the GOSAT SIF Lite files do not  
190 contain the footprint latitude and longitude vertices, whereas the OCO-2/3 SIF Lite files do.

191

192 The *Metadata* group houses variables with sounding-level metadata information, including build version  
193 of the data, unique orbit and sounding identifiers, and measurement mode.

194

195 The *Meteo* group contains meteorological forecast variables, which were obtained from the GEOS-5 FP-IT  
196 3h forecast (Lucchesi, 2015) and are provided as-is without validation. The *Offset* group is a collection of  
197 variables of the bias/offset adjustments and statistics. These include mean, median, and standard deviations  
198 of the adjusted and unadjusted SIF values separated by cross-track footprint. These data are reported on a  
199 grid of signal level bins with a range of 3.0-229.0 W/m<sup>2</sup>/s/μm and follows the SIF bias correction scheme  
200 outlined by (Frankenberg et al., 2011b).

### 201 3.2 Quality flag criterion and rationale

202 The *Quality\_Flag* variable indicates the quality of the data for each sounding as being *best* (0), *good* (1), or  
203 *failed* (2). We recommend using a combination of *best* and *good* for scientific analysis. The criterion for  
204 the *best* and *good* quality flags are listed in Table 2, and soundings that do not meet either set of criteria are  
205 flagged as *failed*. The rationale for the criterion is as follows: reduced chi-square ( $\chi^2$ ) thresholds exclude  
206 fits that do not well represent the spectrum; continuum level radiance excludes scenes with brightness that  
207 is too high or low; solar zenith angle ( $\theta$ ) excludes retrievals with extreme solar zenith angles, which are  
208 more likely affected by rotational Raman scattering; and the O<sub>2</sub> and CO<sub>2</sub> thresholds exclude most cloudy  
209 scenes.





## 210 **4 Methods**

### 211 **4.1 SIF retrieval**

212 The SIF values provided in the SIF Lite files are based on spectral fits covering Fraunhofer lines, as SIF  
213 reduces the fractional depth of the Fraunhofer lines (Plascyk, 1975). The SIF retrieval methodologies are  
214 fully explained by Frankenberg et al. (2011b, a) and SIF is retrieved for GOSAT and the OCO platforms at  
215 757 nm and 771 nm. We estimated SIF at 740 nm for each sounding using both retrieval windows as  
216 described in more detail below. The main retrieval quantity in the retrieval state vector is the fractional  
217 contribution of SIF to the continuum level radiance, or relative fluorescence (SIF\_Relative\_757nm and  
218 SIF\_Relative\_771nm). The absolute SIF values (SIF\_757nm and SIF\_771nm) are generated during post-  
219 processing in  $W/m^2/s/\mu m$ .

### 220 **4.2 SIF 740 nm and intersensor comparisons**

221 The spectral window in which SIF retrievals are made depends on the wavelength bands of the platform.  
222 Assuming the spectral shape of SIF is known and invariant, one can convert SIF to a standard reference  
223 wavelength. Here, we use 740 nm as a reference as it corresponds to the 2<sup>nd</sup> SIF peak and is not as strongly  
224 affected by chlorophyll re-absorption as red SIF, thus showing a relatively stable shape at wavelengths  
225 above 740 nm. The differences in the retrieval windows complicate the comparison of SIF retrievals from  
226 different sensors, thus it is useful to provide SIF at a well-defined reference wavelength.

227

228 Although the range of the wavelengths used to retrieve SIF from the various sensors is small (740-771 nm),  
229 absolute fluorescence can vary greatly depending on the spectral window used to retrieve SIF (Joiner et al.,  
230 2013; Köhler et al., 2018; Sun et al., 2018). However, reference far-red SIF emission spectra at the leaf  
231 level indicates that far-red fluorescence spectral shapes are consistent across species (Magney et al., 2019).  
232 Thus, we provide an estimate of absolute  $SIF_{740}$  (SIF\_740nm) in the GOSAT and OCO-2/3 SIF Lite files  
233 derived from the empirical relationship between SIF at 740 nm and SIF at 758.7 nm and 770.1 nm (denoted  
234 as 757 nm and 771 nm; Eq. 1). The rationale for including  $SIF_{740}$  in the SIF Lite files is to allow for more  
235 consistent and robust comparisons of SIF and SIF-based analyses across sensors (Parazoo et al., 2019), and  
236 to reduce the retrieval error by a factor of  $\sqrt{2}$  (Sun et al., 2018).

237

$$238 \quad SIF_{740} = 0.5 \cdot (1.5 \cdot SIF_{757} + 2.25 \cdot SIF_{771}) \quad (1)$$

239

240 We noted that although the empirical ratio of  $SIF_{757}$  and  $SIF_{771}$  is 1.80 based on leaf level measurements  
241 conducted by Magney et al. (2019), we observed a median ratio of 1.45 from OCO-2 over vegetated areas



242 for 2015-2019 (Figure S1). The reason for this difference has not yet been discerned and requires further  
243 analysis, but the small potential bias introduced by the use of the empirical ratio does not infringe on the  
244 utility of the SIF<sub>740</sub> data.

#### 245 **4.3 SIF retrieval uncertainty**

246 The determination of single sounding retrieval uncertainty is covered in great detail by Sun et al. (2018)  
247 and Frankenberg et al. (2014), and is provided in the SIF Lite files as SIF\_Uncertainty\_740nm,  
248 SIF\_Uncertainty\_757nm, and SIF\_Uncertainty\_771nm. Briefly, these values are the 1-sigma ( $\sigma$ ) estimated  
249 single sounding measurement precision and represent the random component of the retrieval errors. It is  
250 derived through standard least-square fitting by evaluating the error covariance matrix:

251

$$252 \quad S_e = (K^T S_0 K)^{-1} \quad (2)$$

253

254

255 where  $K$  is the Jacobian matrix of the least-squares fit, and  $S_0$  is the measurement error covariance matrix,  
256 which characterizes the instrument noise per detector pixel.

257

258 For OCO-2/3, the uncertainty for SIF<sub>757</sub> usually ranges between 0.3 and 0.5 W/m<sup>2</sup>/s/μm, or ~15-50% of the  
259 absolute SIF value. Uncertainties for SIF<sub>771</sub> are slightly higher due to less fluorescence and a relatively less  
260 reduction in the fractional depth of the radiance at 771 nm. Uncertainty for SIF<sub>740</sub> is calculated from SIF<sub>757</sub>  
261 and SIF<sub>771</sub>:

262

$$263 \quad SIF_{Uncertainty_{740}} = 0.5 \cdot \sqrt{\left( (1.5 \cdot SIF_{Uncertainty_{757}})^2 + (2.25 \cdot SIF_{Uncertainty_{771}})^2 \right)} \quad (3)$$

264

#### 265 **4.4 Bias/offset correction**

266 Biases in retrieved SIF can occur due to uncertainties in the exact instrument line-shape per footprint or  
267 slight uncertainties in detector linearity. To correct for biases, we use reference targets that are non-  
268 fluorescent surfaces barren of vegetation, similar to the method described by Frankenberg (2011b). In short,  
269 the background signal over reference targets is subtracted from all relative SIF values. We calculate the  
270 background signal for each day as mean SIF over all barren surfaces within a 31-day window centred on  
271 the current day for GOSAT and a 3-day window for OCO-2/3. Here, we identify barren surfaces using a  
272 combination of the MODIS MCD12Q1 land cover data product (Friedl and Sulla-Menashe, 2019) and the



273 Vegetation Photosynthesis Model (VPM) (Xiao et al., 2004; Zhang et al., 2017) from the year 2018. The  
274 native spatial resolution of these data sets is 500 m, but we aggregated the data to a global 0.20-degree grid  
275 so that the barren surface reference targets had a coarser resolution than the soundings. We classified barren  
276 surfaces as those grid cells which were 100% barren and/or snow and ice by MCD12Q1 and had zero (0)  
277 annual gross primary production as estimated by VPM. We also excluded coastal grid cells that overlapped  
278 with water using a global coastline shapefile and a buffer.

#### 279 **4.5 Daily average SIF and the daily correction factor**

280 We provide an estimate of daily average SIF (Daily\_SIF), which is instantaneous SIF scaled entirely upon  
281 the geometry of incoming solar radiation over a day. Instantaneous SIF is the absolute value of SIF for any  
282 given sounding and is a strong function of the illumination of the canopy at that instant in time. The  
283 differences in the illumination geometry of soundings at different overpass times and latitudes complicate  
284 direct comparisons of SIF at different points of Earth's surface and comparisons of SIF to other data that  
285 are more temporally coarse, such as daily estimates of GPP.

286

287 Downwelling solar radiation scales linearly with  $\cos(\theta)$  under clear sky conditions when ignoring Rayleigh  
288 scattering and gas absorption. As described by Frankenberg et al. (2011b) and Köhler et al. (2018), a first  
289 order approximation of daily average SIF ( $SIF_{Daily}$ ) can be written as:

$$290 \quad SIF_{Daily} = SIF_{t_0} \cdot \frac{1}{\cos(\theta(t_0))} \cdot \int_{t=t_0-12h}^{t=t_0+12h} \cos(\theta(t)) \cdot H(\cos(\theta(t))) dt \quad (4)$$

291 ere  $SIF_{t_0}$  is absolute instantaneous SIF,  $\theta(t_0)$  is the solar zenith angle  $\theta$  at the time of measurement  $t_0$  with  
292 a heaviside function  $H$  to zero out negative values of  $\cos(\theta)$ , and the integral is computed numerically  
293 in 10-min time steps ( $dt$ ). In terms of the SIF Lite file variable names, this equation can be written for SIF  
294 at any wavelength as  $Daily\_SIF = SIF \cdot daily\_correction\_factor$ .

## 295 **5 Discussion**

### 296 **5.1 Scaling of SIF to GPP**

297 We should note that SIF is, to first order, only a proxy for the electron transfer rate in the light reaction of  
298 photosystem II. However, SIF is oblivious to the light-independent reactions that fix  $CO_2$ . Nevertheless,  
299 many studies have reported on the linearity of SIF and GPP at bi-weekly or monthly timescales and at  
300 coarse spatial resolutions (Verma et al., 2017; Doughty et al., 2019; Yang et al., 2015). The seasonality of  
301 SIF and GPP tend to match well at such coarse temporal resolutions because both SIF and GPP are being  
302 driven by changes in canopy structure, the amount chlorophyll in the canopy, and the amount of sunlight  
303 (photosynthetically active radiation; PAR) being absorbed by canopy chlorophyll ( $APAR_{chl}$ ) (Magney et



304 al., 2020; Doughty et al., 2021; Dechant et al., 2019). The SIF-GPP relationship can also become more  
305 linear at the canopy scale due to the contribution of total canopy SIF by sunlit, shaded, stressed, and non-  
306 stressed leaves (Magney et al., 2019). SIF and GPP have an indirect relationship through non-  
307 photochemical quenching and the electron transport rate (Porcar-Castell et al., 2014; Gu et al., 2019), which  
308 can sometimes simultaneously downregulate photosynthesis and SIF, as has been seen in evergreen  
309 needleleaf ecosystems, but not always (Magney et al., 2019).

310

311 At the leaf level, GPP saturates before SIF in response to APAR, such that we could see increased SIF  
312 without any response in GPP at high levels of APAR (Gu et al., 2019). Conversely, vegetation stress can  
313 cause a near or total cessation of GPP via stomatal closure with little or no change in SIF. This decoupling  
314 has been seen at the leaf scale during forced stomatal closure of deciduous tree species (Marrs et al., 2020)  
315 and a 1-month drought experiment with Eastern cottonwood (*Populus deltoides*) (Helm et al., 2020).  
316 However, these studies and others of deciduous vegetation and croplands have repeatedly found a better  
317 correlation between SIF and APAR than SIF and GPP (Yang et al., 2018; Miao et al., 2018). For SIF to be  
318 a reliable proxy of APAR,  $SIF_{yield}$  (ratio of SIF to APAR) would need to remain constant. For a detailed  
319 inquiry into SIF and photosynthesis, see Porcar-Castell et al. (2014), and a review of SIF remote sensing  
320 applications and challenges from the leaf, tower, and satellite scale by Magney et al. (2020) and Mohammed  
321 et al. (2019).

## 322 **5.2 Negative SIF values**

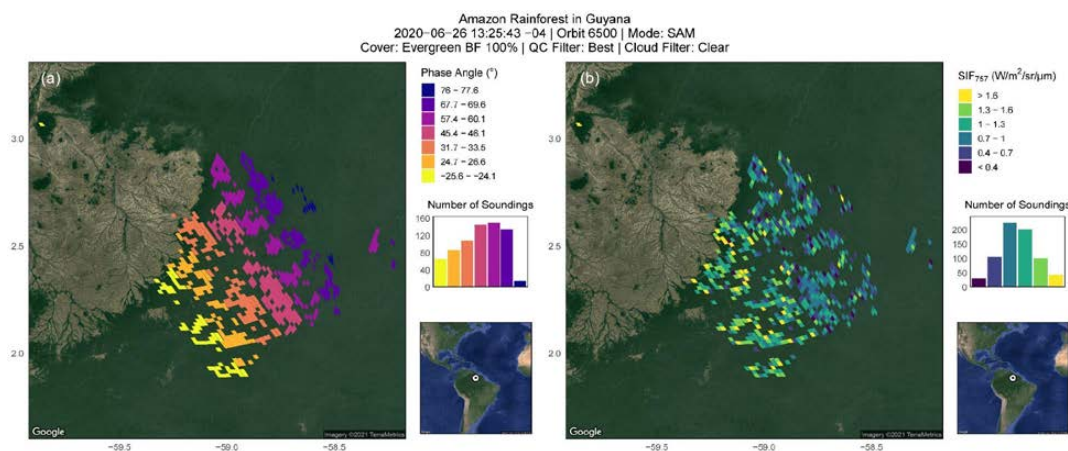
323 Data users are likely to find negative SIF values, which are due to retrieval noise, but these values should  
324 generally not be discarded. The one-sigma uncertainty in retrieved SIF values ( $SIF_{Uncertainty}$ ) can be  
325 substantial, but negative values are plausible in a retrieval sense although not in physical terms (actual SIF  
326 emission cannot be negative). Discarding negative values will introduce a high bias when averaging.  
327 Nevertheless, extremely negative values may indicate a problem with the retrieval. We recommend the  
328 following guidelines for filtering negative SIF values: accept if  $SIF + 2\sigma \text{ uncertainty} \geq 0$ ; questionable if  
329  $SIF + 2\sigma \text{ uncertainty} < 0$  and  $SIF + 3\sigma \text{ uncertainty} \geq 0$ ; and reject if  $SIF + 3\sigma \text{ uncertainty} < 0$ . These  
330 thresholds have not been incorporated into the `Quality_Flag` variable of the SIF Lite data.

## 331 **5.3 Sun-sensor geometry**

332 Users of SIF data from any source should be aware that sun-sensor geometry plays a role in the absolute  
333 values of SIF, in addition to vegetation canopy characteristics (Joiner et al., 2020; Köhler et al., 2018).  
334 Absolute SIF values increase rapidly when the phase angle approaches  $0^\circ$  (when the sun and sensor are  
335 aligned), but the effect of sun-sensor geometry has been shown to be small when the phase angle is greater

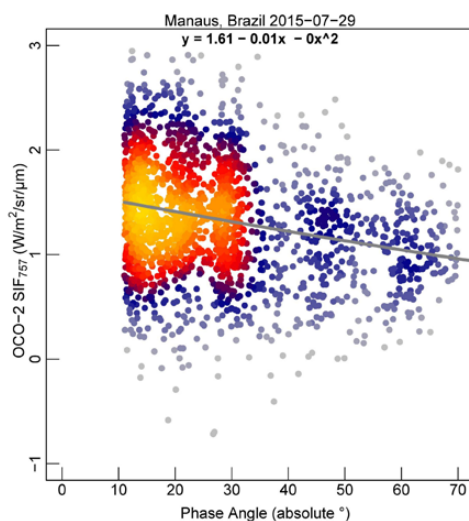


336 than  $20^\circ$  (Köhler et al., 2018; Doughty et al., 2019). Thus, retrieved SIF values from target or SAM mode  
337 scans during a single overpass can vary greatly despite homogeneous vegetation cover due to changing sun-  
338 sensor geometries during data acquisition. Figure 3 illustrates the phase angle and  $SIF_{757}$  for a SAM  
339 acquired over the Amazon rainforest, where the vegetation canopy is very homogenous. The figure also  
340 illustrates how the phase angle changes during an OCO-3 SAM scan and that the sun-sensor geometries for  
341 each individual swath are rather distinct from each other (Figure 3a). Mean SIF for each swath is also  
342 distinctively different (Figure 3b), despite that the canopy was experiencing the same illumination geometry  
343 and environmental conditions during the two minutes in which this SAM was acquired. The effect of sun-  
344 sensor geometry is also illustrated in Figure 4, which shows the relationship between SIF for individual  
345 OCO-2 soundings and phase angle for two target scans in the Amazon. A distinctive change in the absolute  
346 values of retrieved SIF were observed due to sun-sensor geometry.  
347



348  
349 **Figure 3. Phase angle and  $SIF_{757}$  for an OCO-3 SAM mode scan over the Amazon Rainforest in**  
350 **Guyana.** OCO-3 SAMs are composed of several scans of a target whereby the eight-sounding wide swath  
351 is offset adjacent to the previous scan. Each swath has a distinctive, small range of phase angles as seen in  
352 (a). SIF has higher values at lower phase angles, which is apparent in (b) where the higher SIF values  
353 occur for the soundings in the southwestern portion of the SAM where phase angles are lowest.  
354





355

356 **Figure 4. Absolute phase angle and SIF<sub>757</sub> for an OCO-2 target mode scan over evergreen broadleaf**  
357 **forest in Manaus, Brazil.** As this figure demonstrates, retrieved SIF values increase as the phase angle  
358 approaches 0 degrees.

#### 359 5.4 Averaging over space and time to reduce retrieval uncertainty

360 There are two main challenges to working with all spaceborne SIF data: 1) the inherently large uncertainties  
361 for individual soundings due to retrieval noise, and 2) the effect of differences in sun-sensor geometry on  
362 retrieved SIF values. Thus, we advise against using single soundings for analysis. However, averaging  
363 soundings across space and time can reduce the retrieval noise by a factor of  $1/\sqrt{n}$ , with  $n$  being the number  
364 of soundings comprising the average (Frankenberg et al., 2014). For platforms with a wide swath, like the  
365 TROPospheric Monitoring Instrument (TROPOMI), the effect of sun-sensor geometry can be accounted  
366 for by averaging soundings for a point of interest over the entire repeat cycle (16-days for TROPOMI) as  
367 demonstrated by Doughty et al. (2019, 2021). In the case of OCO-2/3, as we demonstrate in Figure 3 and  
368 in Braghieri et al. (2021), soundings can be grouped by phase angle and then averaged to reduce retrieval  
369 uncertainty. Thus, retrieval uncertainty and sun-sensor geometry effects can be substantially minimized.  
370 For GOSAT, we recommend averaging SIF retrieved from both the P and S polarizations, as demonstrated  
371 in Figure 5.

372

373 Users should also keep in mind that when conducting analyses at large spatial scales, gridding the data prior  
374 to analysis is largely unnecessary as the ungridded Level 2 data can be used directly (Doughty et al., 2019).  
375 Doing so will allow the users to retain sounding-level information that may aid in the interpretation of the  
376 results, which would otherwise be lost when merely gridding the SIF values.



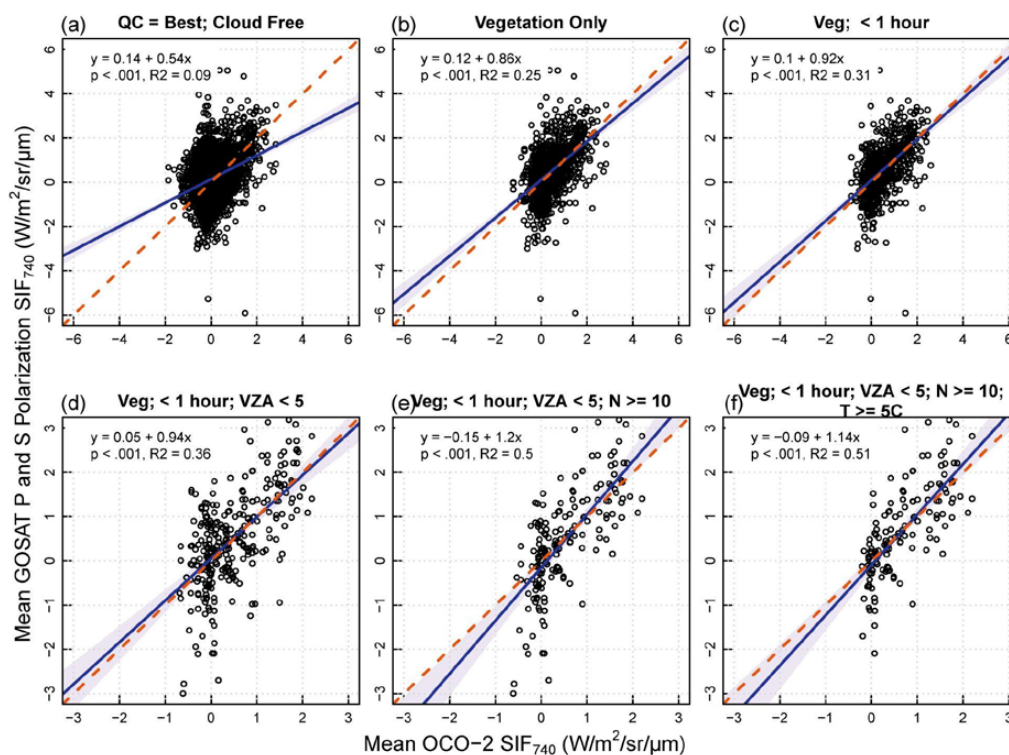
### 377 **5.5 The use of SIF at 740, 757, and 771 nm**

378 It is important to note that in areas where the SIF signal is weak, the use of  $SIF_{757}$  at would be more  
379 appropriate as the SIF signal is stronger at this wavelength. In areas where vegetation is sparse or  $SIF_{yield}$  is  
380 low due to vegetation responses to environmental conditions or canopy leaf physiology,  $SIF_{771}$  could be  
381 within the noise range due to its relatively far distance from the far-red peak at 740 nm. In these cases, we  
382 advise the use of  $SIF_{757}$ . Since  $SIF_{771}$  is used to compute  $SIF_{740}$  in the SIF Lite files, diligence should  
383 likewise be used when using  $SIF_{740}$  in analyses.

### 384 **5.6 Comparison of GOSAT, OCO-2, and OCO-3**

385 OCO-3 SIF has been shown to have a very high correlation ( $r > 0.9$ ) with OCO-2 (Taylor et al., 2020).  
386 Here, we present the first comparisons between GOSAT and OCO-2 Level 2 data. Currently, there are not  
387 enough coincident soundings for GOSAT and OCO-3 to provide a robust analysis but given that OCO-2  
388 and OCO-3 compare very well, we would expect a comparison between GOSAT and OCO-3 to mimic the  
389 findings from our GOSAT and OCO-2 comparison.

390  
391 Although the data record for GOSAT and OCO-2 overlap six years, only a small percentage of soundings  
392 flagged as best quality and cloud free from GOSAT and OCO-2 overlap on the same day (Figure 5a).  
393 Despite this filter, the mean SIF values may differ widely on the same day due to differences in overpass  
394 time (and thus solar illumination angle and environmental conditions), viewing geometry, and the number  
395 of OCO-2 soundings comprising the mean. We progressively filtered the data as illustrated in Figure 5 to  
396 ensure the soundings were of a vegetated land surface, had similar sun-sensor geometries, environmental,  
397 and atmospheric conditions, and that the temperature was high enough for photosynthesis to occur.



398

399 **Figure 5. Relationships of SIF<sub>740</sub> from OCO-2 and GOSAT using progressively conservative data**  
 400 **filters and Deming regression.** X-axis values are the mean of all OCO-2 soundings (~1.3 km by 2.25  
 401 km) that fall within the corresponding GOSAT sounding footprint (~10 km in diameter). Y-axis values  
 402 represent the mean of SIF retrieved from P and S polarizations for a single GOSAT sounding. Six years  
 403 of data (2015-2020) were used to identify soundings that overlapped on the same day. (a) Soundings  
 404 flagged as best quality and cloud free. (b) Same as (a) but filtered as being over vegetation using the  
 405 IGBP flag in the OCO-2 SIF Lite file. (c) Same as (b) but filtered for data that was acquired from GOSAT  
 406 and OCO-2 within one hour of each other. (d) Same as (c) but with viewing zenith angles (VZA) < 5° for  
 407 both platforms. (e) Same as (d) but with number (N) of OCO-2 soundings within a GOSAT sounding  
 408 being ≥ 10. (f) Same as (e) but with skin temperature ≥ 5 °C.

409

410 We found that the correlation and slope improved with more conservative filtering of the data, and that the  
 411 comparison between GOSAT SIF and OCO-2 SIF were reasonable. However, it is important to note that  
 412 any comparison between GOSAT and OCO data will inevitably be affected by spatial sampling bias, as the  
 413 swath width for both OCO platforms is smaller than the diameter of the GOSAT footprints (Figure 6; left  
 414 footprints). Also, it could be the case that only a small portion of the GOSAT footprint is sampled by OCO

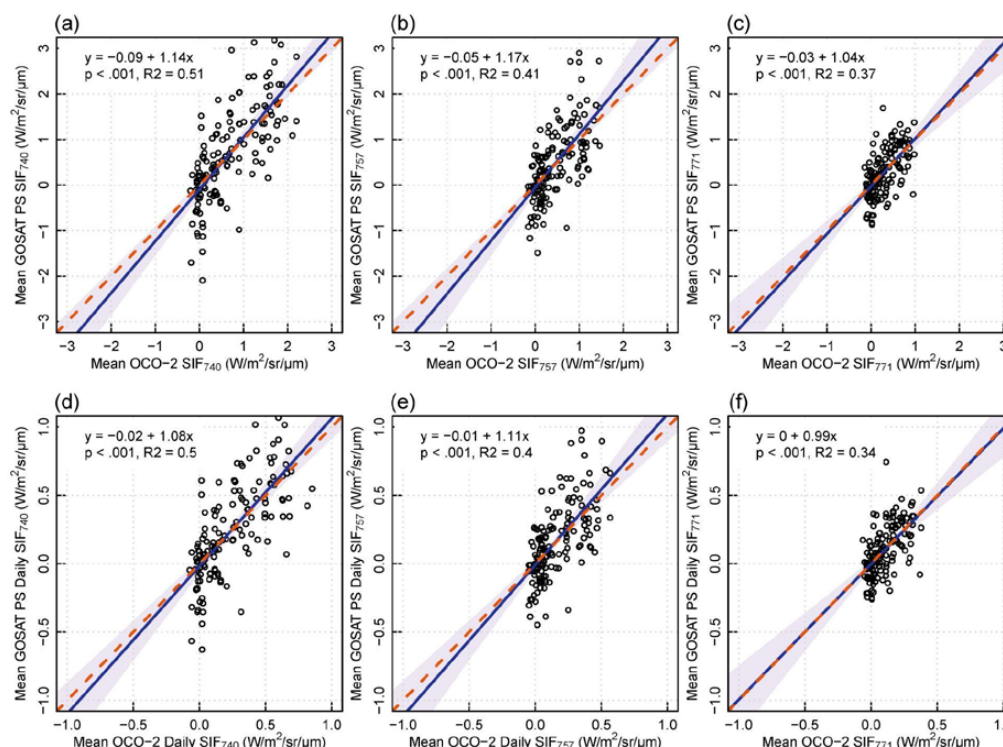


415 (Figure 6; right footprints). Our filter of  $\geq 10$  OCO-2 soundings within a GOSAT footprint aimed to reduce  
416 this potential sampling bias in addition to reducing the uncertainty of the OCO-2 SIF retrievals. It must also  
417 be remembered that in this comparison, we do not have the luxury to average several GOSAT soundings to  
418 reduce the uncertainty as we did with OCO-2, so the uncertainties of the GOSAT SIF is much higher than  
419 that for OCO-2.  
420



421  
422 **Figure 6. Overlapping GOSAT and OCO-2 soundings near Quill Lakes, Saskatchewan, Canada.**  
423 Orange circles are GOSAT sounding footprints (~10 km) and the white rhomboids are OCO-2 sounding  
424 footprints (~1.3 km by 2.25 km) acquired on the same day as the GOSAT soundings in which they fall.  
425 The GOSAT and OCO-2 soundings on the left were acquired in February 2019, and the soundings on the  
426 right were acquired in July 2017. The base map is a Google Satellite image.

427  
428 Upon a more detailed comparison of GOSAT and OCO-2 SIF at 740 nm, 757 nm, and 771 nm using the  
429 strictest filter we applied in Figure 5f, we found  $SIF_{740}$  from the two platforms to have higher correlations  
430 than for  $SIF_{757}$  and  $SIF_{771}$  alone (Figure 7). We also noticed that GOSAT and OCO-2 soundings most  
431 frequently overlap in the boreal winter, which corresponds to a period of little or no photosynthesis at mid  
432 and high latitudes (Figures S2 and S3). Thus, the direct comparison of GOSAT and OCO-2 SIF is severely  
433 restricted by the relatively infrequent overlap of the two platforms during the growing season.



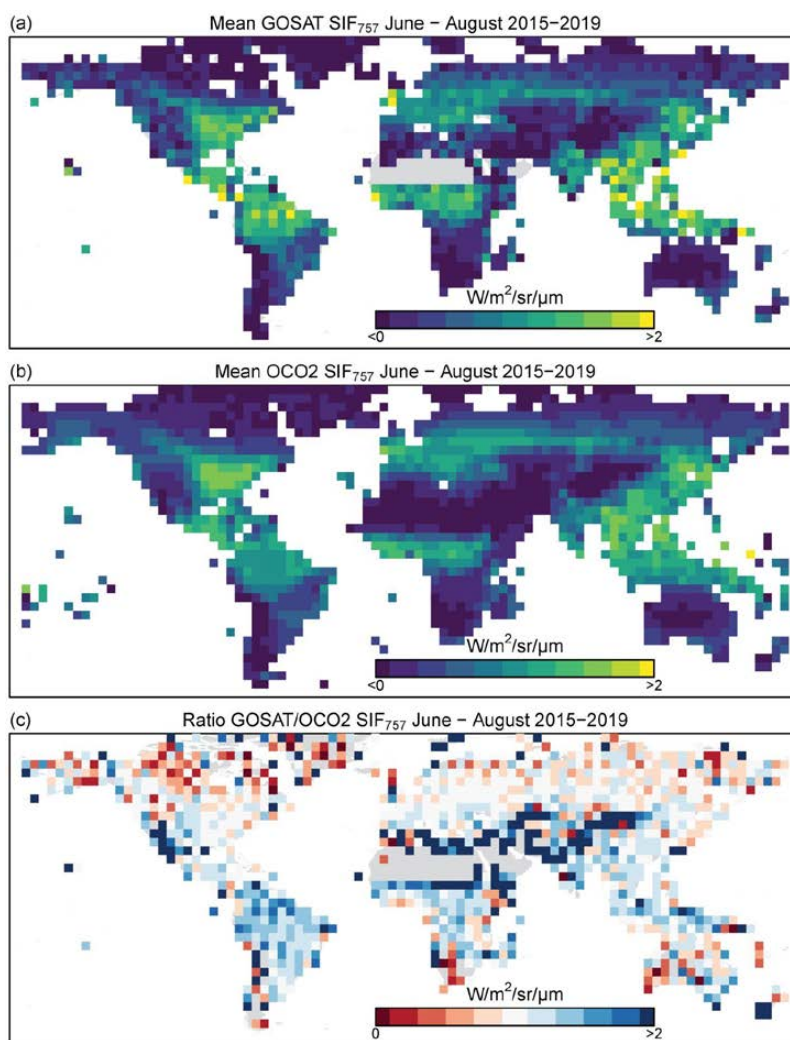
434

435 **Figure 7. Relationships between SIF<sub>740</sub>, SIF<sub>757</sub>, and SIF<sub>771</sub> from GOSAT and OCO-2 using Deming**  
436 **regression.** The soundings presented here were those presented in main text Figure 5f, which were data  
437 that had the most conservative filter: best quality and cloud free, vegetation, co-occurring within 1 hour,  
438 viewing zenith angle < 5°, number of OCO-2 soundings within a GOSAT footprint ≥ 10, and skin  
439 temperature ≥ 5 °C.

440

441 In addition to the sounding level comparisons, we found mean annual SIF<sub>757</sub> for GOSAT and  
442 OCO-2 to compare reasonably well at the global scale during the boreal summer (Figure 8). The  
443 relatively large differences in SIF illustrated at the gridcell level in Figure 8c are due to differences in the  
444 spatial and temporal sampling of the two platforms.





445

446 **Figure 8. Mean GOSAT to OCO-2 SIF<sub>740</sub> and their ratio at 4.0 degrees for June-August 2015-2019.**

447

### 448 **5.7 Collocating Soundings with their Targets**

449 Currently, the target and SAM soundings are not collated to the target to which they correspond, but  
450 variables will be added to future versions of the SIF Lite files that will allow for the collocation of target  
451 and SAM soundings with their intended target site. For OCO-3, some of the target sites are in close  
452 proximity to each other and thus a target site may fall within the scan of another target. For these sites, users  
453 may also want to check scans that were intended for target sites adjacent to their target of interest. The



454 OCO-3 targets, the dates of their scans, and scan maps are available at  
455 <https://ocov3.jpl.nasa.gov/sams/index.php>. A list of target locations for OCO-2 and OCO-3 are available in  
456 Table S1 and Table S2, respectively.

## 457 **6 Conclusions**

458 Users of remote sensing data are more accustomed to using Level 3 gridded data for analyses, but we  
459 incentivize data users to also exploit the Level 2 data we have presented in the SIF Lite files. The OCO-2  
460 and OCO-3 platforms provide the highest spatial resolution spaceborne SIF data, and the target and SAM  
461 observation modes are unique to these platforms. The observation scheme for the OCO platforms allow for  
462 time series to be constructed for the target locations, and the repeated target and SAM scans allow for the  
463 investigation of the directionality and escape of SIF at varying sun-sensor geometries across many biomes  
464 in different seasons.

465

466 We have demonstrated how users can break target and SAM observations into phase angles for analysis  
467 and have described how the effect of sun-sensor geometry and retrieval noise can be mitigated through the  
468 averaging of the data. The OCO platforms also provide a rich resource for the validation of radiative transfer  
469 models, which is currently underutilized. Upcoming spaceborne platforms with frequent revisits and/or  
470 high spatial resolution, such as the FLuorescence EXplorer (FLEX) by the European Space Agency and  
471 NASA's Geostationary Carbon Cycle Observatory (GeoCarb), are expected to further our understanding of  
472 changes in vegetation structure and function (Drusch et al., 2016; Polonsky et al., 2014; Moore et al., 2018).

## 473 **7 Data availability**

474 All SIF Lite files presented here can be found at NASA Goddard Earth Sciences (GES) Data and  
475 Information Services Center (DISC) at <https://disc.gsfc.nasa.gov/datasets/>. OCO-2 can be accessed at  
476 <https://doi.org/10.5067/XO2LBBNPO010>, and OCO-3 data can be accessed at  
477 [https://disc.gsfc.nasa.gov/datacollection/OCO3\\_L2\\_Lite\\_SIF\\_EarlyR.html](https://disc.gsfc.nasa.gov/datacollection/OCO3_L2_Lite_SIF_EarlyR.html). Links to other SIF data  
478 products are listed at NASA Jet Propulsion Lab (JPL) website for SIF at  
479 <https://climatesciences.jpl.nasa.gov/sif/>.

## 480 **8 Author contributions**

481 RD and CF conceived this manuscript. TK prepared and provided the data and RD performed the  
482 analysis. RD prepared the manuscript with contributions from all co-authors.



483 **9 Competing interests**

484 The authors declare that they have no conflict of interest.

485 **10 Acknowledgements**

486 We thank Lan Dang for helping to process the GOSAT data and Annmarie Eldering for helping coordinate  
 487 the publication of the SIF Lite files at the GES-DISC.

488 **11 Financial support**

489 This research was supported by NASA Making Earth System Data Records for Use in Research  
 490 Environments (MEaSUREs) Program (NNN12AA01C) and the NASA OCO Science Team  
 491 (80NSSC18K0895).

492

493 **Table 1. Level 2 GOSAT, OCO-2, and OCO-3 SIF Lite netCDF File Global Attributes, Dimensions,**  
 494 **and Variables.** Units for SIF and continuum level radiance variables are  $W/m^2/sr/\mu m$ , geolocation variables  
 495 are in decimal degrees, angles are in degrees, and the units for the meteorological variables are in the table  
 496 below. For GOSAT, data is provided for both the P and S polarizations as a 2-dimensional array. \* denotes  
 497 the variable or dimension is only applicable to OCO-2 and OCO-3, and \*\* denotes that the dimension is  
 498 only applicable to GOSAT. Note that there are different MeasurementMode and OrbitID descriptions for  
 499 GOSAT, and that some root-level variables are duplicated in the Geolocation and Science group.

Global Attributes	
date_time_coverage	UTC time string of the first and last observation
day_of_year_coverage	Same as date_time_coverage, but with day-of-year
InputCollectionLabel	Collection label of the L2 data products used to create the file
InputBuildID	Build ID of the L2 data products used to create the file
InputPointers	String with names of all input products and auxiliary data used to create the file
Dimensions (length of dimension)	
sounding_dim (variable)	Number of soundings in the file
footprint_dim (8) *	Number of OCO-2/3 across-track footprints
vertex_dim (4) *	Number of footprint corner coordinates
signalbin_dim (227)	Number of entries in the signal histogram arrays in the Offset group
statistics_dim (2)	Array dimension in the Mean and Median SIF values of the Offset group; adjusted and unadjusted values
polarization_dim (2) **	Array dimension of the polarization for GOSAT; P and S polarization



Root Level Variables	
Daily_SIF_740nm	Daily Corrected Solar induced chlorophyll fluorescence at 740 nm: $\text{Daily\_SIF\_740nm} = \text{SIF\_740} * / \text{Science/daily\_correction\_factor}$
Daily_SIF_757nm	Daily Corrected Solar induced chlorophyll fluorescence at 757 nm: $\text{Daily\_SIF\_757nm} = / \text{Science/sif\_757nm} * / \text{Science/daily\_correction\_factor}$
Daily_SIF_771nm	Daily Corrected Solar induced chlorophyll fluorescence at 771 nm: $\text{Daily\_SIF\_771nm} = / \text{Science/sif\_771nm} * / \text{Science/daily\_correction\_factor}$
Delta_Time	Timestamp (seconds since 1 January 1990)
Latitude	Center latitude of the measurement
Latitude_Corners *	Corner latitude of the measurement
Longitude	Center longitude of the measurement
Longitude_Corners *	Corner longitude of the measurement
Quality_Flag	0 = best (passes quality control + cloud fraction = 0.0); 1 = good (passes quality control); 2 = bad (failed quality control); -1 = not investigated
SAz	Azimuth angle between the solar direction as defined by the sounding location, and the sounding local north
SIF_740nm	Solar induced chlorophyll fluorescence at retrieved wavelength: $\text{SIF\_740nm} = 0.75 * (/ \text{Science/sif\_757nm} + 1.5 * / \text{Science/sif\_771nm})$
SIF_Uncertainty_740nm	Uncertainty computed from continuum level radiance at 740 nm: $\text{SIF\_Uncertainty\_740} = 0.75 * ((/ \text{Science/sif\_757nm})^2 + (1.5 * / \text{Science/sif\_771nm})^2)^{1/2}$
SZA	Solar zenith angle is the angle between the line of sight to the sun and the local vertical
VAz	Azimuth angle between line of sight and local north
VZA	Sensor zenith angle is the angle between the line of sight to the sensor and the local vertical
<u>Variable/Group Name</u>	<u>Description</u>
Cloud Group Variables	
cloud_flag_abp	Indicator of whether the sounding contained clouds: 0 - Classified clear, 1 - Classified cloudy, 2 - Not classified, all other values undefined; not used in SIF Lite processing
co2_ratio	Ratio of CO2 retrieved in weak and strong CO2 band (value near 1 indicate scattering free scene)
delta_pressure_abp	Retrieved-predicted surface pressure from ABO2, usable as cloud screener; not used in SIF Lite processing
o2_ratio	Ratio of retrieved and predicted O2 column
surface_albedo_abp	Surface albedo (Lambertian equivalent) as retrieved in the ABO2 preprocessor at 760nm; not used in SIF processing
Geolocation Group Variables	
altitude	Surface altitude of observed footprint
footprint_latitude_vertices *	Latitude corner coordinates of the sounding location
footprint_longitude_vertices *	Longitude corner coordinates of the sounding location



latitude	Center latitude of the measurement
longitude	Center longitude of the measurement
sensor_azimuth_angle	Azimuth angle between line of sight and local north
sensor_zenith_angle	Sensor zenith angle is the angle between the line of sight to the sensor and the local vertical
solar_azimuth_angle	Azimuth angle between the solar direction as defined by the sounding location, and the sounding local north
solar_zenith_angle	Solar zenith angle is the angle between the line of sight to the sun and the local vertical
time_tai93	Timestamp (seconds since 1 January 1993)
<b>Metadata Group Variables</b>	
BuildID	The ID of the Build, including the software version that created this product
CollectionLabel	The Collection Label of the Build, including the software version that created this product
FootprintID *	OCO-2 footprint identifier (1-8), identifying the 8 independent OCO-2 spatial samples per frame
MeasurementMode	OCO-2/3: Instrument Measurement Mode, 0=Nadir, 1=Glint, 2=Target, 3=AreaMap, 4=Transition; users might consider separating these for analysis  GOSAT: Instrument Measurement Mode, 0=OB1D (FTS obs. mode I, sunlit), 1=OB2D (FTS obs mode II, sunlit), 2=SPOD (FTS specific obs. mode, sunlit); users might consider separating these for analysis
OrbitID	Orbit Identifier: Start Orbit Number (OCO-2) or Start Solar Day (OCO-3) of observation  GOSAT: Orbit Identification String ("NominalDay OrbitOfDay StartPathNumber-StopPathNumber")
SoundingID	Unique Identifier for each sounding
<b>Meteo (Meteorological) Group Variables</b>	
specific_humidity	Specific humidity at surface layer at the sounding location, interpolated from GEOS-5 FP-IT inst3_3d_asm_Nv field QV (specific_humidity); kg/kg
surface_pressure	Surface pressure at the sounding location; interpolated from GEOS-5 FP-IT inst3_3d_asm_Nv field PS (surface_pressure); Pa
temperature_skin	Skin temperature at the sounding location; interpolated from GEOS-5 FP-IT inst3_2d_asm_Nx field TS (surface_skin_temperature); K
temperature_two_meter	Two-meter temperature at the sounding location; interpolated from GEOS-5 FP-IT inst3_2d_asm_Nx field T2M (2-meter_air_temperature); K
vapor_pressure_deficit	Vapor pressure deficit at the sounding location (2m) (ECMWF forecast); Pa
wind_speed	Surface wind speed at sounding location; interpolated from GEOS-5 FP-IT inst3_2d_asm_Nx field U10M and inst3_2d_asm_Nx field V10M (10-meter_eastward_wind, 10-meter_northward_wind); m/s
<b>Offset Group Variables</b>	
SIF_Mean_757nm	Mean Solar Induced Fluorescence at 757nm (by footprint, for adjusted and unadjusted values)





SIF_Mean_771nm	Mean Solar Induced Fluorescence at 771nm (by footprint, for adjusted and unadjusted values)
SIF_Median_757nm	Median Solar Induced Fluorescence at 757nm (by footprint, for adjusted and unadjusted values)
SIF_Median_771nm	Median Solar Induced Fluorescence at 771nm (by footprint, for adjusted and unadjusted values)
SIF_Relative_Mean_757nm	Mean relative Solar Induced Fluorescence at 757nm (by footprint, for adjusted and unadjusted values)
SIF_Relative_Mean_771nm	Mean relative Solar Induced Fluorescence at 771nm (by footprint, for adjusted and unadjusted values)
SIF_Relative_Median_757nm	Median relative Solar Induced Fluorescence at 757nm (by footprint, for adjusted and unadjusted values)
SIF_Relative_Median_771nm	Median relative Solar Induced Fluorescence at 771nm (by footprint, for adjusted and unadjusted values)
SIF_Relative_SDev_757nm	Standard deviation of relative Solar Induced Fluorescence at 757nm (by footprint, for adjusted and unadjusted values)
SIF_Relative_SDev_771nm	Standard deviation of relative Solar Induced Fluorescence at 771nm (by footprint, for adjusted and unadjusted values)
signal_histogram_757nm	Signal level histogram for 757 nm radiances
signal_histogram_771nm	Signal level histogram for 771 nm radiances
signal_histogram_bins	Radiance level offset histogram bins
<b>Science Group Variables</b>	
continuum_radiance_757nm	Continuum Level Radiance at 757 nm
continuum_radiance_771nm	Continuum Level Radiance at 771 nm
daily_correction_factor	Correction factor to estimate daily average SIF from instantaneous SIF (using pure geometric incoming light scaling)
IGBP_index *	IGBP Index
SIF_757nm	Offset-Adjusted Solar Induced Chlorophyll Fluorescence at 757nm
SIF_771nm	Offset-Adjusted Solar Induced Chlorophyll Fluorescence at 771nm
SIF_Relative_757nm	Relative Solar Induced Fluorescence at 757 nm
SIF_Relative_771nm	Relative Solar Induced Fluorescence at 771 nm
SIF_Unadjusted_757nm	Solar Induced Chlorophyll Fluorescence at 757nm, no offset adjustment
SIF_Unadjusted_771nm	Solar Induced Chlorophyll Fluorescence at 771nm, no offset adjustment
SIF_Unadjusted_Relative_757nm	Solar Induced Chlorophyll Fluorescence at 757nm in fractions of continuum level, no offset adjustment
SIF_Unadjusted_Relative_771nm	Solar Induced Chlorophyll Fluorescence at 771nm in fractions of continuum level, no offset adjustment
SIF_Uncertainty_757nm	One-Sigma Statistical Uncertainty in Solar Induced Chlorophyll Fluorescence at 757nm
SIF_Uncertainty_771nm	One-Sigma Statistical Uncertainty in Solar Induced Chlorophyll Fluorescence at 771nm



sounding_land_fraction	Percentage of land surface type within the sounding
sounding_qual_flag	Sounding Quality Flag: 0 = good, 1 = bad

500

501 **Table 2. Criterion of quality flags *best* and *good* for the Level 2 GOSAT, OCO-2, and OCO-3 data.**

502 Soundings that do not meet either set of criteria are flagged as *failed* (2).

Quality_Flag = 0 ( <i>best</i> )	Quality_Flag = 1 ( <i>good</i> )
$28 \leq \text{continuum radiance @757nm} \leq 195$ [W/m <sup>2</sup> /sr/μm]	$28 \leq \text{continuum radiance @757nm} \leq 195$ [W/m <sup>2</sup> /sr/μm]
$\chi^2 @ 757\text{nm} \leq 2.0$	$\chi^2 @ 757\text{nm} \leq 3.0$
$\chi^2 @ 771\text{nm} \leq 2.0$	$\chi^2 @ 771\text{nm} \leq 3.0$
$0.85 \leq \text{O}_2 \text{ ratio} \leq 1.5$	$0.85 \leq \text{O}_2 \text{ ratio} \leq 1.5$
$0.5 \leq \text{CO}_2 \text{ ratio} \leq 4.0$	$0.5 \leq \text{CO}_2 \text{ ratio} \leq 4.0$
$\theta_{\text{sun}} \leq 80^\circ$ for GOSAT; $\theta_{\text{sun}} \leq 70^\circ$ for OCO-2/3	$\theta_{\text{sun}} \leq 80^\circ$ for GOSAT; $\theta_{\text{sun}} \leq 70^\circ$ for OCO-2/3
Land Fraction = 100%	Land Fraction $\geq 80\%$

503

504

505 **References**

506 Braghieri, R. K., Wang, Y., Doughty, R., Sousa, D., Magney, T., Widlowski, J.-L., Longo, M., Bloom, A.  
 507 A., Worden, J., and Gentine, P.: Accounting for canopy structure improves hyperspectral radiative  
 508 transfer and sun-induced chlorophyll fluorescence representations in a new generation Earth System  
 509 model, 261, 112497, 2021.

510 Crisp, D., Pollock, H. R., Rosenberg, R., Chapsky, L., Lee, R. A., Oyafuso, F. A., Frankenberg, C.,  
 511 O'Dell, C. W., Bruegge, C. J., and Doran, G. B.: The on-orbit performance of the Orbiting Carbon  
 512 Observatory-2 (OCO-2) instrument and its radiometrically calibrated products, 10, 59–81, 2017.

513 Dechant, B., Ryu, Y., Badgley, G., Zeng, Y., Berry, J. A., Zhang, Y., Goulas, Y., Li, Z., Zhang, Q., and  
 514 Kang, M.: Canopy structure explains the relationship between photosynthesis and sun-induced  
 515 chlorophyll fluorescence in crops, 2019.

516 Doughty, R., Köhler, P., Frankenberg, C., Magney, T. S., Xiao, X., Qin, Y., Wu, X., and Moore, B.:  
 517 TROPOMI reveals dry-season increase of solar-induced chlorophyll fluorescence in the Amazon forest,  
 518 201908157, 2019.

519 Doughty, R., Xiao, X., Köhler, P., Frankenberg, C., Qin, Y., Wu, X., Ma, S., and Moore III, B.: Global-  
 520 scale consistency of spaceborne vegetation indices, chlorophyll fluorescence, and photosynthesis,  
 521 e2020JG006136, 2021.

522 Drusch, M., Moreno, J., Del Bello, U., Franco, R., Goulas, Y., Huth, A., Kraft, S., Middleton, E. M.,  
 523 Miglietta, F., and Mohammed, G.: The fluorescence explorer mission concept—ESA's earth explorer 8,  
 524 55, 1273–1284, 2016.

525 Eldering, A., Taylor, T. E., O'Dell, C. W., and Pavlick, R.: The OCO-3 mission: measurement objectives  
 526 and expected performance based on 1 year of simulated data., 12, 2019.



- 527 Frankenberg, C., Butz, A., and Toon, G. C.: Disentangling chlorophyll fluorescence from atmospheric  
528 scattering effects in O2 A-band spectra of reflected sun-light, 38, 2011a.
- 529 Frankenberg, C., Fisher, J. B., Worden, J., Badgley, G., Saatchi, S. S., Lee, J.-E., Toon, G. C., Butz, A.,  
530 Jung, M., and Kuze, A.: New global observations of the terrestrial carbon cycle from GOSAT: Patterns of  
531 plant fluorescence with gross primary productivity, 38, 2011b.
- 532 Frankenberg, C., O'Dell, C., Berry, J., Guanter, L., Joiner, J., Köhler, P., Pollock, R., and Taylor, T. E.:  
533 Prospects for chlorophyll fluorescence remote sensing from the Orbiting Carbon Observatory-2, 147, 1–  
534 12, 2014.
- 535 Frankenberg, C., Köhler, P., Magney, T. S., Geier, S., Lawson, P., Schwochert, M., McDuffie, J., Drewry,  
536 D. T., Pavlick, R., and Kuhnert, A.: The Chlorophyll Fluorescence Imaging Spectrometer (CFIS),  
537 mapping far red fluorescence from aircraft, 217, 523–536, 2018.
- 538 Friedl, M. and Sulla-Menashe, D.: MCD12Q1 MODIS/Terra+ aqua land cover type yearly L3 global  
539 500m SIN grid V006 [data set], 10, 2019.
- 540 Genty, B., Briantais, J.-M., and Baker, N. R.: The relationship between the quantum yield of  
541 photosynthetic electron transport and quenching of chlorophyll fluorescence, 990, 87–92, 1989.
- 542 Gu, L., Han, J., Wood, J. D., Chang, C. Y.-Y., and Sun, Y.: Sun-induced Chl fluorescence and its  
543 importance for biophysical modeling of photosynthesis based on light reactions, 223, 1179–1191, 2019.
- 544 Guanter, L., Alonso, L., Gómez-Chova, L., Amorós-López, J., Vila, J., and Moreno, J.: Estimation of  
545 solar-induced vegetation fluorescence from space measurements, 34, 2007.
- 546 Helm, L. T., Shi, H., Lerdau, M. T., and Yang, X.: Solar-induced chlorophyll fluorescence and short-term  
547 photosynthetic response to drought, 30, e02101, 2020.
- 548 Joiner, J., Yoshida, Y., Vasilkov, A. P., and Middleton, E. M.: First observations of global and seasonal  
549 terrestrial chlorophyll fluorescence from space, 8, 637–651, 2011.
- 550 Joiner, J., Guanter, L., Lindstrot, R., Voigt, M., Vasilkov, A. P., Middleton, E. M., Huemmrich, K. F.,  
551 Yoshida, Y., and Frankenberg, C.: Global monitoring of terrestrial chlorophyll fluorescence from  
552 moderate-spectral-resolution near-infrared satellite measurements: methodology, simulations, and  
553 application to GOME-2, 6, 2803–2823, 2013.
- 554 Joiner, J., Yoshida, Y., Köehler, P., Campbell, P., Frankenberg, C., van der Tol, C., Yang, P., Parazoo, N.,  
555 Guanter, L., and Sun, Y.: Systematic Orbital Geometry-Dependent Variations in Satellite Solar-Induced  
556 Fluorescence (SIF) Retrievals, Remote Sensing, 12, 2346, 2020.
- 557 Köhler, P., Frankenberg, C., Magney, T. S., Guanter, L., Joiner, J., and Landgraf, J.: Global retrievals of  
558 solar induced chlorophyll fluorescence with TROPOMI: first results and inter-sensor comparison to  
559 OCO-2, 2018.
- 560 Kuze, A., Suto, H., Nakajima, M., and Hamazaki, T.: Thermal and near infrared sensor for carbon  
561 observation Fourier-transform spectrometer on the Greenhouse Gases Observing Satellite for greenhouse  
562 gases monitoring, 48, 6716–6733, 2009.
- 563 Lucchesi, R.: File Specification for GEOS-5 FP-IT. GMAO Office Note No. 2 (Version 1.3), 2015.
- 564 Magney, T. S., Frankenberg, C., Köhler, P., North, G., Davis, T. S., Dold, C., Dutta, D., Fisher, J. B.,  
565 Grossmann, K., and Harrington, A.: Disentangling changes in the spectral shape of chlorophyll



- 566 fluorescence: Implications for remote sensing of photosynthesis, 124, 1491–1507, 2019.
- 567 Magney, T. S., Barnes, M. L., and Yang, X.: On the covariation of chlorophyll fluorescence and  
568 photosynthesis across scales, 47, e2020GL091098, 2020.
- 569 Marrs, J. K., Reblin, J. S., Logan, B. A., Allen, D. W., Reinmann, A. B., Bombard, D. M., Tabachnik, D.,  
570 and Hutrya, L. R.: Solar-Induced Fluorescence Does Not Track Photosynthetic Carbon Assimilation  
571 Following Induced Stomatal Closure, 47, e2020GL087956, 2020.
- 572 Maxwell, K. and Johnson, G. N.: Chlorophyll fluorescence—a practical guide, 51, 659–668, 2000.
- 573 Miao, G., Guan, K., Yang, X., Bernacchi, C. J., Berry, J. A., DeLucia, E. H., Wu, J., Moore, C. E.,  
574 Meacham, K., and Cai, Y.: Sun-induced chlorophyll fluorescence, photosynthesis, and light use efficiency  
575 of a soybean field from seasonally continuous measurements, 123, 610–623, 2018.
- 576 Mohammed, G. H., Colombo, R., Middleton, E. M., Rascher, U., van der Tol, C., Nedbal, L., Goulas, Y.,  
577 Pérez-Priego, O., Damm, A., and Meroni, M.: Remote sensing of solar-induced chlorophyll fluorescence  
578 (SIF) in vegetation: 50 years of progress, 231, 111177, 2019.
- 579 Moore, B., Crowell, S., Rayner, P., Kumer, J., O’Dell, C., O’Brien, D., Utembe, S., Polonsky, I., Schimel,  
580 D., and Lemen, J.: The potential of the geostationary carbon cycle observatory (GeoCarb) to provide  
581 multi-scale constraints on the carbon cycle in the Americas, 6, 109, 2018.
- 582 Müller, N. J. C.: Beziehungen zwischen assimilation, absorption und fluoreszenz im chlorophyll des  
583 lebenden blattes, 9, 42–49, 1874.
- 584 OCO-2 Science Team, Gunson, M., and Eldering, A.: OCO-2 Level 2 bias-corrected solar-induced  
585 fluorescence and other select fields from the IMAP-DOAS algorithm aggregated as daily files,  
586 Retrospective processing VEarlyR, <https://doi.org/10.5067/XO2LBBNPO010>, 2020.
- 587 OCO-3 Science Team, Gunson, M., and Eldering, A.: OCO-3 Level 2 bias-corrected solar-induced  
588 fluorescence and other select fields from the IMAP-DOAS algorithm aggregated as daily files,  
589 Retrospective processing VEarlyR,  
590 [https://disc.gsfc.nasa.gov/datacollection/OCO3\\_L2\\_Lite\\_SIF\\_EarlyR.html](https://disc.gsfc.nasa.gov/datacollection/OCO3_L2_Lite_SIF_EarlyR.html), 2020.
- 591 Parazoo, N. C., Frankenberg, C., Köhler, P., Joiner, J., Yoshida, Y., Magney, T., Sun, Y., and Yadav, V.:  
592 Towards a harmonized long-term spaceborne record of far-red solar-induced fluorescence, 124, 2518–  
593 2539, 2019.
- 594 Plascyk, J. A.: The MK II Fraunhofer line discriminator (FLD-II) for airborne and orbital remote sensing  
595 of solar-stimulated luminescence, 14, 144339, 1975.
- 596 Polonsky, I. N., O’Brien, D. M., Kumer, J. B., and O’Dell, C. W.: Performance of a geostationary  
597 mission, geoCARB, to measure CO<sub>2</sub>, CH<sub>4</sub> and CO column-averaged concentrations, 7, 959–981, 2014.
- 598 Porcar-Castell, A., Tyystjärvi, E., Atherton, J., Van der Tol, C., Flexas, J., Pfündel, E. E., Moreno, J.,  
599 Frankenberg, C., and Berry, J. A.: Linking chlorophyll a fluorescence to photosynthesis for remote  
600 sensing applications: mechanisms and challenges, 65, 4065–4095, 2014.
- 601 Schreiber, U., Schliwa, U., and Bilger, W.: Continuous recording of photochemical and non-  
602 photochemical chlorophyll fluorescence quenching with a new type of modulation fluorometer, 10, 51–  
603 62, 1986.
- 604 Sun, Y., Frankenberg, C., Wood, J. D., Schimel, D. S., Jung, M., Guanter, L., Drewry, D. T., Verma, M.,



- 605 Porcar-Castell, A., and Griffis, T. J.: OCO-2 advances photosynthesis observation from space via solar-  
606 induced chlorophyll fluorescence, 358, eaam5747, 2017.
- 607 Sun, Y., Frankenberg, C., Jung, M., Joiner, J., Guanter, L., Köhler, P., and Magney, T.: Overview of  
608 Solar-Induced chlorophyll Fluorescence (SIF) from the Orbiting Carbon Observatory-2: Retrieval, cross-  
609 mission comparison, and global monitoring for GPP, 209, 808–823, 2018.
- 610 Taylor, T. E., Eldering, A., Merrelli, A., Kiel, M., Somkuti, P., Cheng, C., Rosenberg, R., Fisher, B.,  
611 Crisp, D., and Basilio, R.: OCO-3 early mission operations and initial (vEarly) XCO<sub>2</sub> and SIF retrievals,  
612 251, 112032, 2020.
- 613 Verma, M., Schimel, D., Evans, B., Frankenberg, C., Beringer, J., Drewry, D. T., Magney, T., Marang, I.,  
614 Hutley, L., and Moore, C.: Effect of environmental conditions on the relationship between solar-induced  
615 fluorescence and gross primary productivity at an OzFlux grassland site, 122, 716–733, 2017.
- 616 Xiao, X., Hollinger, D., Aber, J., Goltz, M., Davidson, E. A., Zhang, Q., and Moore, B.: Satellite-based  
617 modeling of gross primary production in an evergreen needleleaf forest, 89, 519–534, 2004.
- 618 Yang, K., Ryu, Y., Dechant, B., Berry, J. A., Hwang, Y., Jiang, C., Kang, M., Kim, J., Kimm, H., and  
619 Kornfeld, A.: Sun-induced chlorophyll fluorescence is more strongly related to absorbed light than to  
620 photosynthesis at half-hourly resolution in a rice paddy, 216, 658–673, 2018.
- 621 Yang, X., Tang, J., Mustard, J. F., Lee, J.-E., Rossini, M., Joiner, J., Munger, J. W., Kornfeld, A., and  
622 Richardson, A. D.: Solar-induced chlorophyll fluorescence that correlates with canopy photosynthesis on  
623 diurnal and seasonal scales in a temperate deciduous forest, 42, 2977–2987, 2015.
- 624 Zhang, Y., Xiao, X., Wu, X., Zhou, S., Zhang, G., Qin, Y., and Dong, J.: A global moderate resolution  
625 dataset of gross primary production of vegetation for 2000–2016, 4, 170165, 2017.